

## Supporting Information

### **Influence of Rate of Radiation Energy on Charge-Carrier Kinetics Application of All-Inorganic CsPbBr<sub>3</sub> Perovskite Nanocrystal**

Virendra Kumar<sup>1</sup>, Vandana Nagal<sup>2</sup>, Rahul Kumar<sup>1</sup>, Shubhda Srivastava<sup>3,4</sup>, Bipin Kumar Gupta<sup>4</sup>, Mahesh Kumar<sup>4</sup>, Aurangzeb Khurram Hafiz<sup>2</sup>, Kedar Singh<sup>1\*</sup>

<sup>1</sup>Nanotechnology Lab, School of Physical Sciences, Jawaharlal Nehru University (JNU), New Delhi-110067, India.

<sup>2</sup>Quantum and Nanophotonics Research Laboratory, Centre for Nanoscience and Nanotechnology, Jamia Millia Islamia (A Central University), New Delhi-110025, India.

<sup>3</sup>Academy of Scientific and Innovative Research (AcSIR), Dr. K. S. Krishnan Road, New Delhi-110012, India.

<sup>4</sup>CSIR – National Physical Laboratory, Dr. K. S. Krishnan Road, New Delhi-110012, India.

Email Id: [kedarbhu08@gmail.com](mailto:kedarbhu08@gmail.com); [virendra2181@gmail.com](mailto:virendra2181@gmail.com)

### Analysis explanation of XRD data

X-ray powder diffraction (XRD) is a prompt sophisticated characterization technique used for the phase recognition of crystalline material and can furnish information on dimensions of the unit cell. The PXRD pattern along with indexing according to its bulk orthorhombic counterpart of the as-prepared resulting all-inorganic colloidal CsPbBr<sub>3</sub> PNC as depicted in the **Figure S1 [1]** and include the diffraction peaks such as (100), (110), (111), (200), (210), (211), (220), et cetera, facets of the orthorhombic phase resulting from high reaction temperature and high surface energy during synthesis [2]. The pattern of X-ray diffraction asserts that the orthorhombic space group Pbnm is formed for perovskite structure [3].

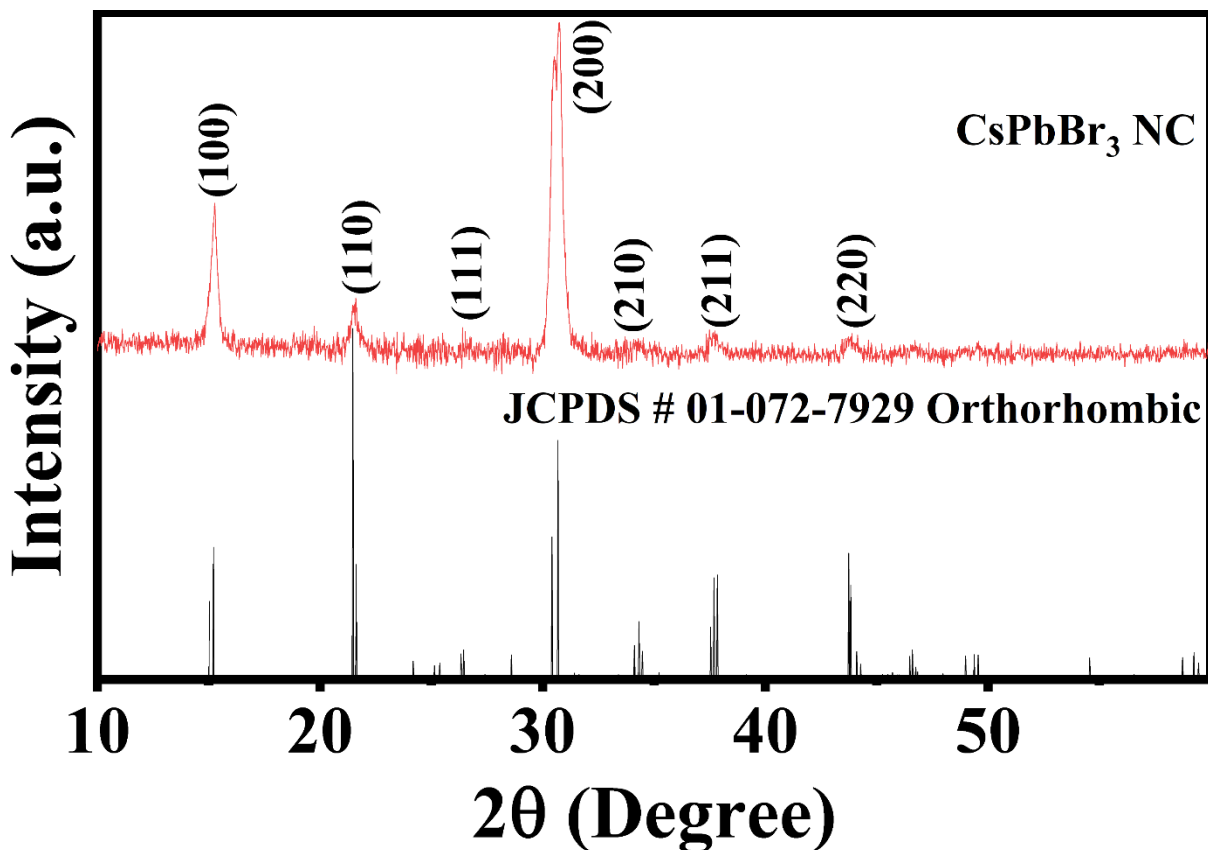


**Figure S1.** X-ray diffraction pattern of the PNC. The pattern comprehended is representing to the artefact of orthorhombic phase.

## Transmission Electron Spectroscopy (TEM)

As depicted in **Figure S2a**, in which (110) plane of the cubic bulk CsPbBr<sub>3</sub> (Powder Diffraction File Card No.# 01-072-7929, a = 0.820700 nm, b = 0.825500 nm, and c = 0.175909 nm) corresponds to the lattice with spacing 0.41nm of all-inorganic colloidal CsPbBr<sub>3</sub> PNC [4]. **Figure S2b** exhibits a pattern that displays the planes (100), (111) and (200), and so forth, of the as-synthesized perovskite of cubic crystal structure [3] and claiming the size of the NC is  $11.58 \pm 0.21$  nm as pictured in **Figure S2c**.

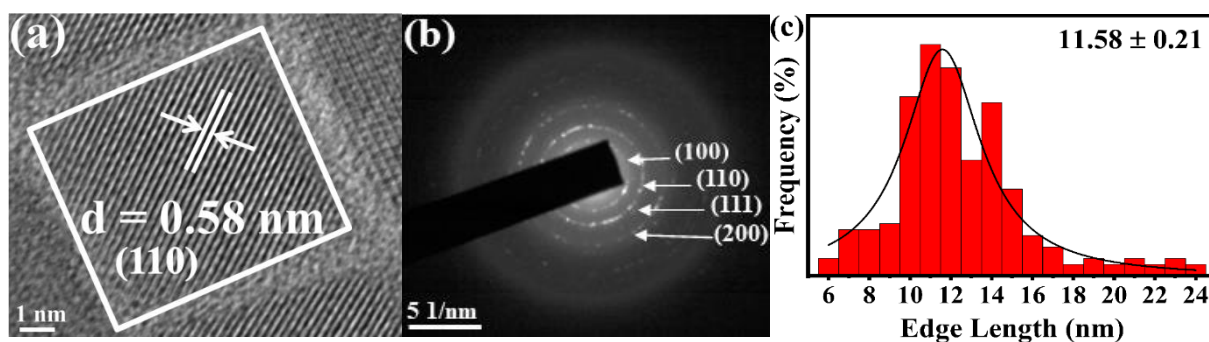


**Figure S2.** Typical TEM images (a) HRTEM; (b) SAED pattern; (c) Size distribution of TEM image of CsPbBr<sub>3</sub> PNC.

## X-ray photoelectron microscopy (XPS)

Likewise, we performed this spectroscopy to acquaint with the stoichiometry of the surface constituents of the PNC. The analysis of the characteristic spectrum of the inorganic perovskite CsPbBr<sub>3</sub> PNC affirms the existence of various kinds of constituents, for instance, cesium, lead, bromine, carbon, nitrogen, and oxygen as shown in **Figure S3** [5]. We have also calculated the elemental compositions with the help of the XPS data as shown in **Table S6**. From the observed results, one can easily comprehend that this PNC has surface composition almost similar to the normal stoichiometric ratio [3]. As displayed in **Figure S4**, the high-resolution core-level spectra of PNC.

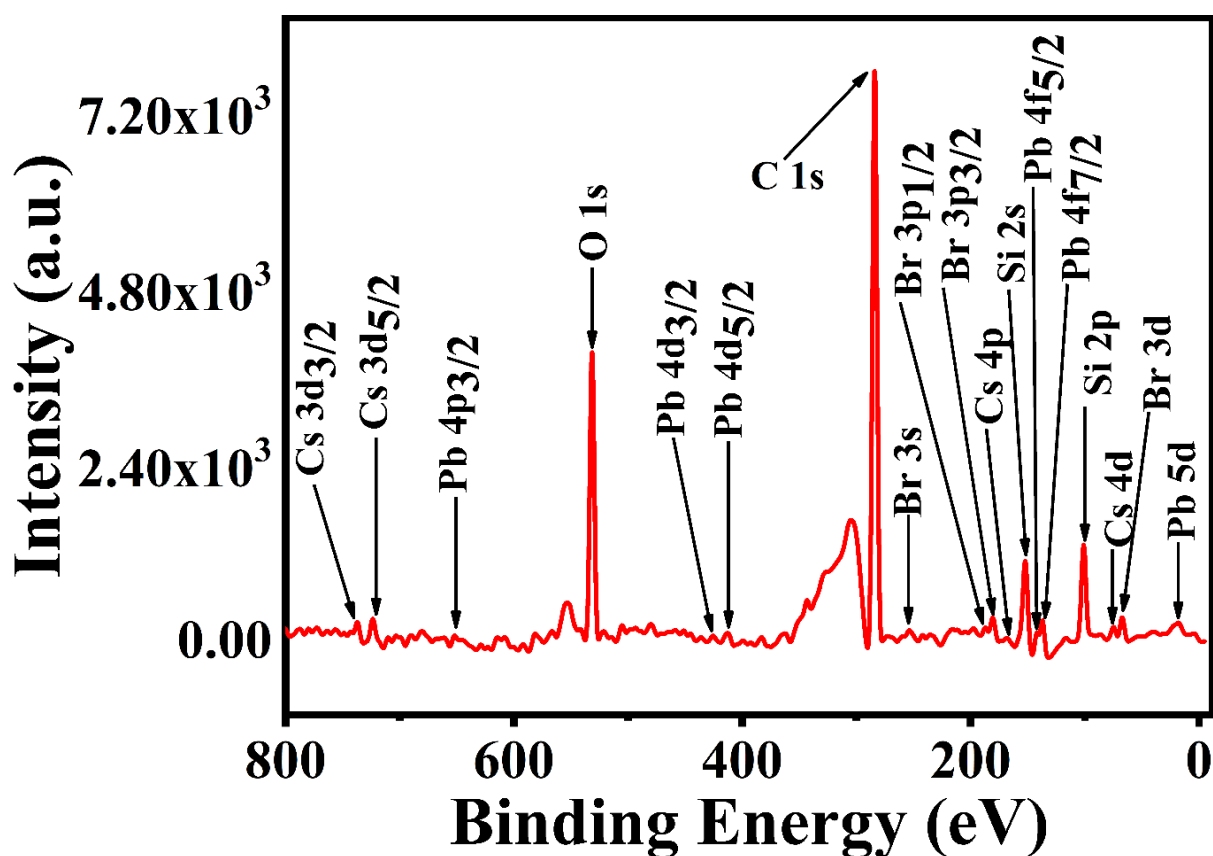


**Figure S3.** The survey spectrum of CsPbBr<sub>3</sub> PNC studied through the X-ray photoelectron spectroscopy (as-synthesized colloidal solution and dispersed in hexane).

The energy of spin-orbit splitting is 13.974 eV, corroborates to the core level peaks Cs 3d<sub>5/2</sub> and Cs 3d<sub>3/2</sub> as depicted in **Figure S4a**, positioned separately at binding energies (E<sub>F</sub>-E) of 724.091 eV and 738.065 eV. Similarly, the energy of spin-orbit splitting is 4.854 eV associated with the core level photoemission features Pb 4f<sub>7/2</sub> and 4f<sub>5/2</sub> as showcased in **Figure S4b**, located separately at binding energies of 137.892 eV and 142.746 eV. The homogeneity and binding energies of spectral shapes convey that Pb depicts the “+2” oxidation state [5]. From **Figure S4b** [6], one can observe that there is no low energy peak (i.e. metallic Pb<sup>0</sup>) present in the high-resolution spectrum of Pb 4f. Prevalence of the Pb ions upon the surface displayed on account of main peaks. Possibility of forming a Pb<sup>2+</sup> oxidation state as a result of the energy of the incident x-ray photon being absorbed by the material which suggests that halide coordination across Pb<sup>2+</sup> might build the octahedral stable structure of PbX<sub>6</sub>. Similarly, as shown in **Figure S4c**, the energy of spin-orbit splitting is 1.031 eV related to the spectra of Br 3d<sub>5/2</sub> and Br 3d<sub>3/2</sub>, localized separately at 68.784 eV and 67.753 eV [7]. Interestingly, the energy of spin-orbit splitting is 2.336 eV associated with two additional peaks which are also present in the spectra, positioned at 74.867 eV and 77.203eV, which accounts for Cs 4d<sub>5/2</sub> and Cs 4d<sub>3/2</sub>, as shown in **Figure S4c** [7]. As shown in **Table S6**, the calculated stoichiometry concerning Cs: Pb: Br becomes 1:1.3:3.3, which corresponding to the binding energy of Br 3d, Pb 4f, and Cs 4d peaks. This further establishes the ionic bonding between Cs<sup>+</sup> and PbBr<sub>6</sub>. Physically one can imagine that Pb- turns less positively charged with more Cs- all-around to donate an electron and less Br accessible to accept an electron. Concurrently, Br- turns highly negatively charged as a result of the surplus electron from Cs [8].

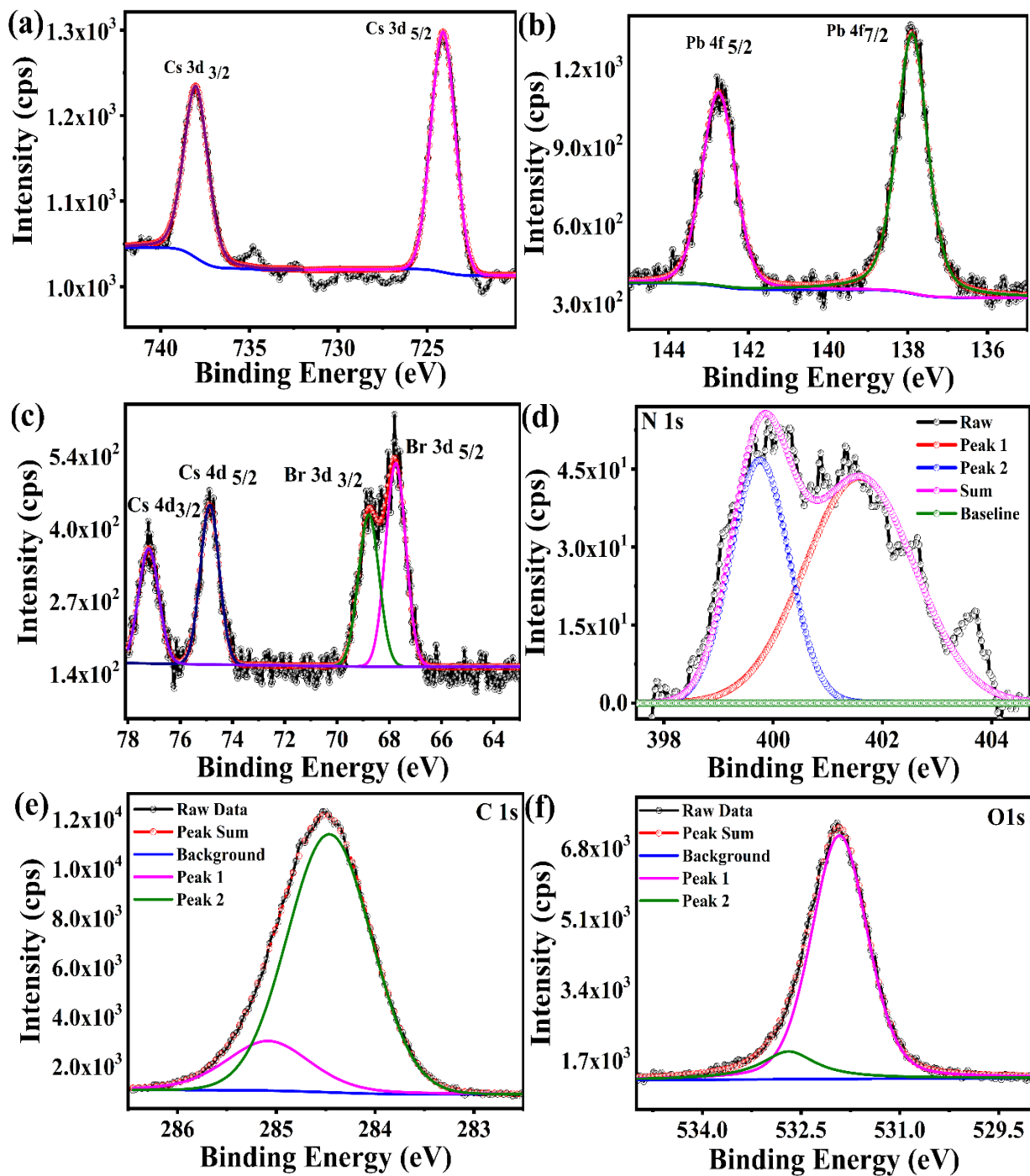


**Figure S4.** Deconvolution of core level photoemission spectrums of (a) Cs 3d, (b) Pb 4f, (c) Cs 4d and Br 3d, (d) N 1s, (e) C 1s, (f) O 1s orbitals, as figure marked, respectively.

The all-inorganic colloidal CsPbBr<sub>3</sub> PNC shows a core level of N 1s that was associated with lower binding energy (~399.8 eV) for free amino alkane groups (-NH<sub>2</sub>) and higher binding energy (~401.6 eV) peak for amino alkane groups (-NH<sub>3</sub><sup>+</sup>) as depicted in the **Figure S4d**. Mostly, the surface of the compound that has been exposed to the atmosphere will have a detectable quantity of carbon contamination. The all-inorganic colloidal CsPbBr<sub>3</sub> PNC shows a core level of N 1s that was associated with lower binding energy (~399.8 eV) for free amino alkane groups (-NH<sub>2</sub>) and higher binding energy (~401.6 eV) peak for amino alkane groups (-NH<sub>3</sub><sup>+</sup>) as depicted in the **Figure S4d**. Mostly, the surface of the compound that has been exposed to the atmosphere will have a detectable quantity of carbon contamination. As shown in **Figure S4e**, it clearly states that C1s core level peaks at (~284.46 eV) which corresponds to the C-C bond, and at (~285.06 eV) which corresponds to C=N bond [9]. With the presence of these two important peaks, one can confirm the peak position of Cs<sup>+</sup> cation as discussed earlier [10]. When exposed to air, oxygen also gets adsorbed, hence, O1s core level peak is also observed as shown in **Figure S4f**, where C-O bonding attributes to (~ 531.9 eV) while the peak at (532.7 eV) can be attributed to H-O-C bonding [3]. These peaks signify the defects in the lattice of CsPbBr<sub>3</sub> PNC. A peak at high binding energy attributed to oxygen vacancy or loosely bound oxygen that was adsorbed on the surface of our sample and low binding energy peak is attributed to O<sub>2</sub> ions defect at intrinsic sites [11].

## Fourier transform infrared (FTIR) spectroscopy

We observed the FTIR spectra of PNC. For the preparation of PNC, OLA is responsible for solubilizing  $\text{PbBr}_2$  salt in the ODE solvent, and OA supports the colloidal dispersion of the following PNC in the non-polar solvent (i.e. hexane) [12]. Both samples (i.e. supernatant and inorganic perovskite  $\text{CsPbBr}_3$  PNC) exhibit FTIR spectra in the range of  $2840\text{-}2960\text{ cm}^{-1}$ , as shown in **Figure S5**. Various stretching vibrations correspond to  $\text{CH}_2$  and  $\text{CH}_3$  for symmetric and asymmetric mode. A signal at  $1466\text{ cm}^{-1}$  which is the distinctive absorption band for the constituents from OA and OLA [13,14] corresponds to the in-plane bending vibration. The signal at  $3078\text{ cm}^{-1}$  indicates the N-H stretching mode and  $\text{NH}_2$  symmetric stretch which is a feature band for OLA, as OLA may be present on the surface of the compounds (i.e. supernatant and  $\text{CsPbBr}_3$  PNC). Symmetric  $\text{NH}_3^+$  deformation can be associated with a sharp peak at  $1641\text{ cm}^{-1}$ , pursuant to the resemblance of N1s at 401.6 eV in the XPS study (explained above). N-H scissor bending vibrations, which is a well-known feature band that comes from the OLA, can be associated with the peak at  $1545\text{ cm}^{-1}$ , confirming on the surface of the compounds (i.e. supernatant and  $\text{CsPbBr}_3$  PNCs), the existence of OLA [12].

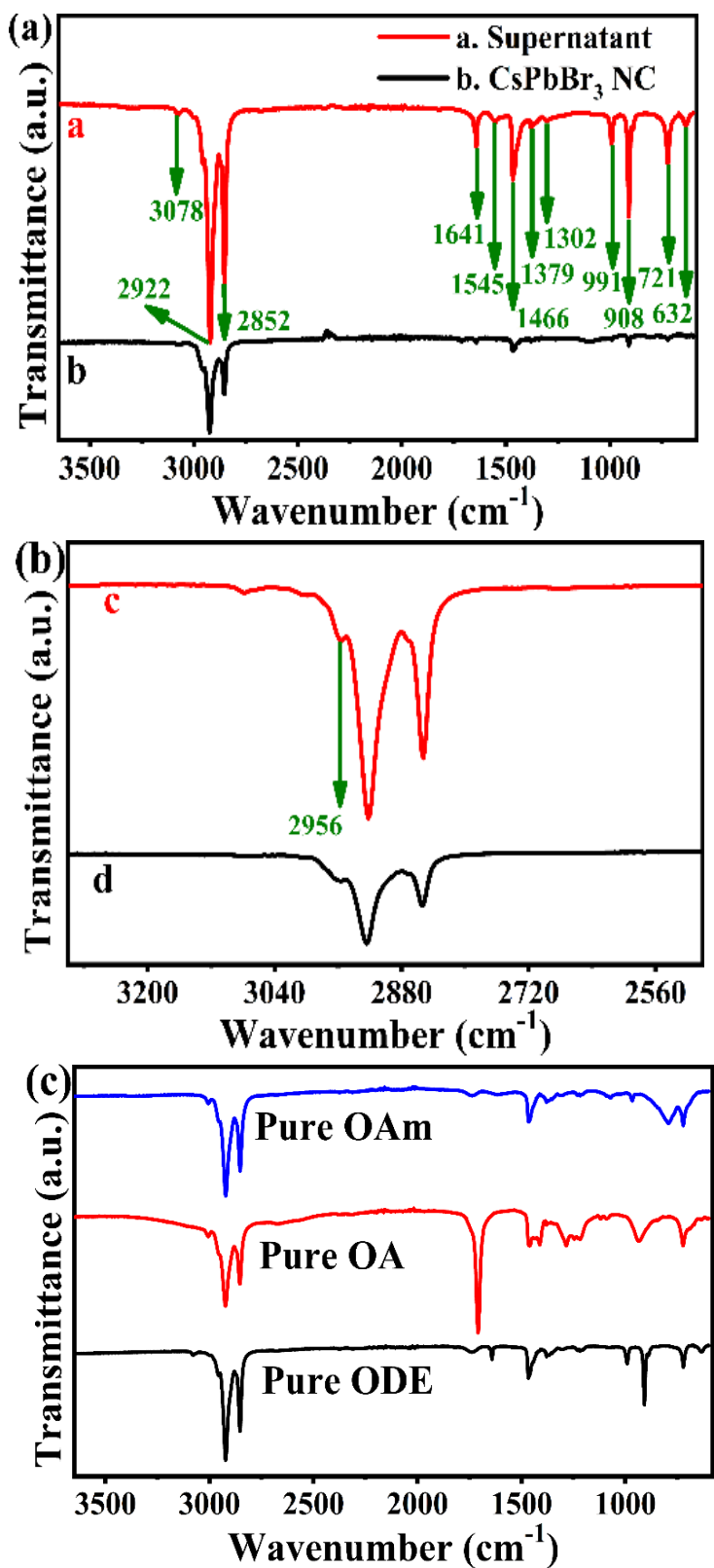


**Figure S5.** Fourier Transform Infrared Spectroscopy (FTIR) of (a) PNC and its supernatant (b) enlarged image of (a); (c) typical ligands and solvent used in this system.

Symmetric C-N and C=O stretching vibrations which come from OLA and OA, can be ascribed to a strong signature at 908 cm<sup>-1</sup> [15]. Another strong peak at 991 cm<sup>-1</sup> is a representation of =C-H i.e. out of plane deformation on the account of ODE. There are two less intense signatures at 1379 cm<sup>-1</sup> and 1302 cm<sup>-1</sup> also found in the spectra of both samples (i.e. PNC and its supernatant), which are representing for the impurities in the prepared samples. While the peak at 720 cm<sup>-1</sup> conforms to the CH-bending and –CH<sub>2</sub> vibration, which is a feature band for OLA, asserting the prevalence of OLA on the surface of the compounds (i.e. supernatant and inorganic CsPbBr<sub>3</sub> PNCs) [16]. Besides, there is a weak signal at 632 cm<sup>-1</sup> designated to =CH<sub>2</sub> twisting vibration which comes from ODE [17]. There is strong quantum confinement that exists into the CsPbBr<sub>3</sub> PNCs just because of ligands attached to the compounds, resulting in not possible to agglomeration and fusion [12].

### **Quantum yield measurement of CsPbBr<sub>3</sub> PNC sample was done as described below**

#### **Introduction**

An integral attribute of a fluorophore is characterized by the PLQYs. The ratio of photons absorbed to photons gives out through photoluminescence attest to the PLQYs.

$$QY = \frac{\text{Photons}_{em}}{\text{Photons}_{abs}}$$

Comparative rates like radiative  $k_r$  and non-radiative  $k_{nr}$  relaxation pathways also demonstrate about the quantum yield  $QY$  expresses by relation given below

$$Q = \frac{k_r}{k_r + \sum k_{nr}}$$

Although quantitative analysis of the absolute quantum yield call for advanced instrumentation, it is more well-to-do to ascertain the comparative quantum yield of CsPbBr<sub>3</sub> PNC by comparing to a reference Fluorescein Dye with the best-known quantum yield. For the comparative

quantum yields quantitative analysis, there are two methods for instance a single point and a relative method. In our work, the relative method has been used on the account of more accuracy into the results although it is a highly time-consuming method. In the case of the relative method, we do a calculation of the slope of the line produced by diagramming the integrated fluorescence intensity against the absorption for multiple concentrations of fluorescence. In this technical representation, Fluorescein Dye which has a fluorescence quantum yield of 0.95, the relative method employed to find out the fluorescence quantum yield of CsPbBr<sub>3</sub> PNC with respect to Fluorescein Dye.

### **Process**

- \* Prepared 5 samples each of Fluorescein Dye and CsPbBr<sub>3</sub> PNC having various absorbance's between 0.01 - 0.1 at the wavelengths of excitation namely 496 nm and 450 nm respectively
- \* At the excitation wavelengths of 496 nm and 450 nm the samples prepared, photoluminescence spectrum from 450 nm to 700 nm measured
- \* The integrated photoluminescence intensity from the spectrum calculated for instance as shown in **Figure S6**
- \* The magnitude of the integrated fluorescence intensity against the absorbance of the solution absorbance diagrammed
- \* Now eventually the quantum yield of photoluminescence spectrum calculated

### **Calculation**

- \* According to this relative method, the photoluminescence quantum yield is estimated practicing the slope of the line find out from the diagram of the absorbance against the integrated photoluminescence intensities. In this instance, the quantum yield can be figured out practicing the below relation-

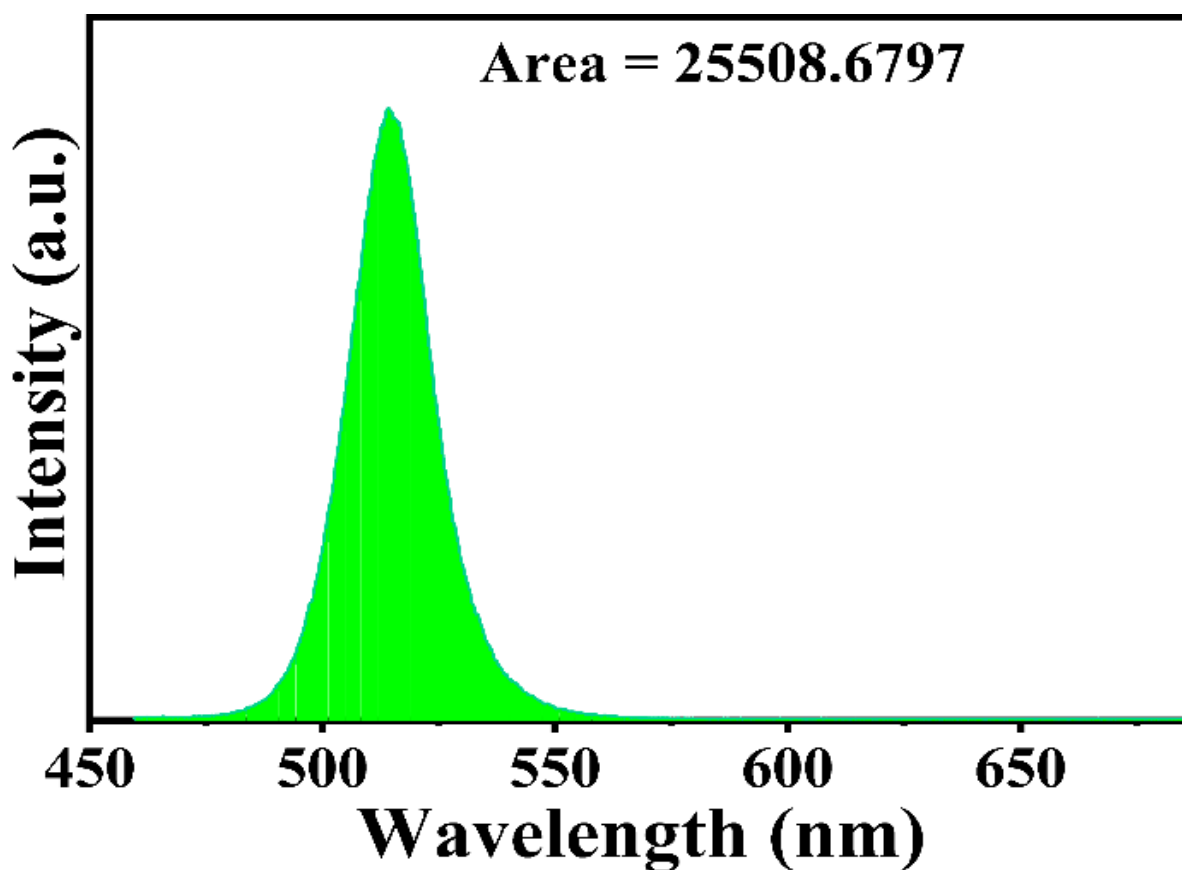


**Figure S6.** The area of the photoluminescence spectrum.

$$QY_{\text{CsPbBr}_3 \text{ NC}} = QY_{\text{Fluorescein Dye}} \left( \frac{m_{\text{CsPbBr}_3 \text{ NC}}}{m_{\text{Fluorescein Dye}}} \right) * \left( \frac{n_{\text{CsPbBr}_3 \text{ NC}}}{n_{\text{Fluorescein Dye}}} \right) \quad (1)$$

- \* Where  $m$  is standing for the slope of the line extracted from the diagram of the integrated photoluminescence intensity vs. absorbance
- \* Refractive index of the respective solvents in which the sample is fully dissolved,  $n$  [2]
- \* Refractive index  $n$  of deionized water 1.330 because the Fluorescein Dye dispersed in it for the 0.1M NaOH solution and the CsPbBr<sub>3</sub> PNC sample dispersed in hexane 1.375
- \* The whole systematic process of calculation of QY of the CsPbBr<sub>3</sub> PNC is elaborated in **Figure S7a-f** and data corresponding to optical densities and area of photoluminescence discussed in **Table S1**

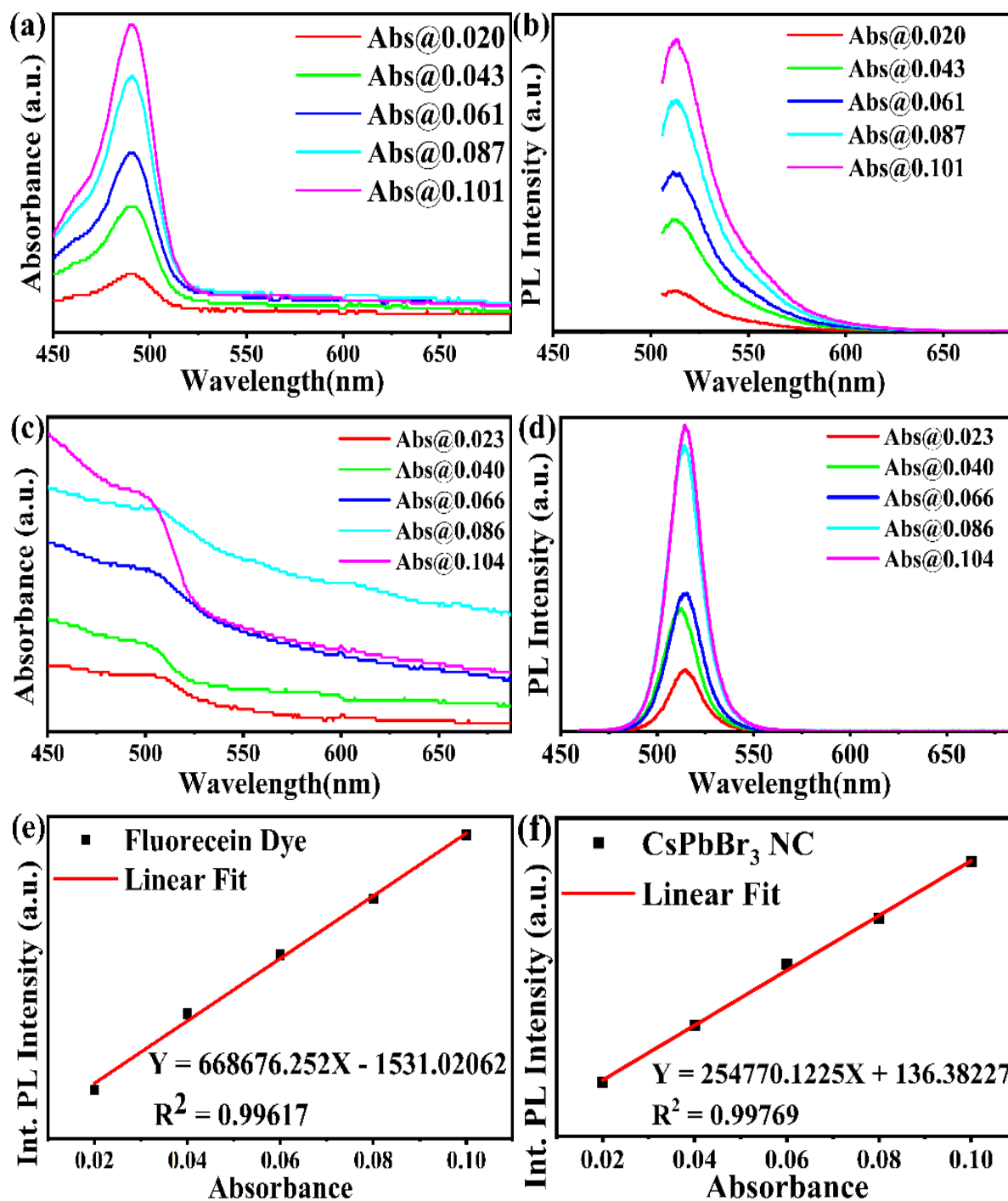


**Figure S7.** (a)-(c) Absorption, (b)-(d) Photoluminescence spectra of Fluorescein Dye and CsPbBr<sub>3</sub> PNC and (e)-(f) Absorbance vs. Area of Photoluminescence.

- \* The  $QY$  value 0.95 well-known (Photoluminescence quantum yield of Fluorescein Dye as a reference) is plugged into the equation (1) above and then ciphered as below [2]

$$\begin{aligned}
 QY_{\text{CsPbBr}_3 \text{ NC}} &= 0.95 * \left( \frac{25508.6797}{65030.1489} \right) * \left( \frac{1.375}{1.330} \right)^2 \\
 &= 0.95 * 0.381 * 1.068 \\
 &= 38.6\%
 \end{aligned}$$

## Urbach Energy

Urbach energy is also one of the ways to know about electronic and structural perturbation inside the crystal lattice as well as on the surface of the crystal lattice. It can be calculated in the region below the edge of the absorption band ( $E < E_g$ ) where it increases exponentially in the case of semiconductors and insulators which is also known as Urbach tail. We plotted the logarithmic of the absorption coefficient at room temperature vs photon energy, as shown in **Figure S8a** [1]. To acquaint with the defects of as-synthesized CsPbBr<sub>3</sub> PNC, we have studied Urbach energy ( $E_U$ ), Urbach tail's exponential part was fitted by applying the following Urbach's rule (Eq. 2),

$$\alpha(E) = \alpha_0 e^{\left[ \sigma(T) \frac{E-E_0}{k_B T} \right]}, \quad (2)$$

or

$$\alpha(E) = \alpha_0 e^{\left[ \frac{E-E_0}{E_U} \right]}, \quad (3)$$

where the absorption coefficient is represented by  $\alpha(E)$ ,  $E_0$  (or  $E_g$ ) and  $\alpha_0$  are the material-specific constants, steepness parameter is  $\sigma(T)$ , Boltzmann constant is  $k_B$  and the absolute temperature is  $T$ , the Urbach energy is given by the relation  $E_U = k_B T / \sigma(T)$ .

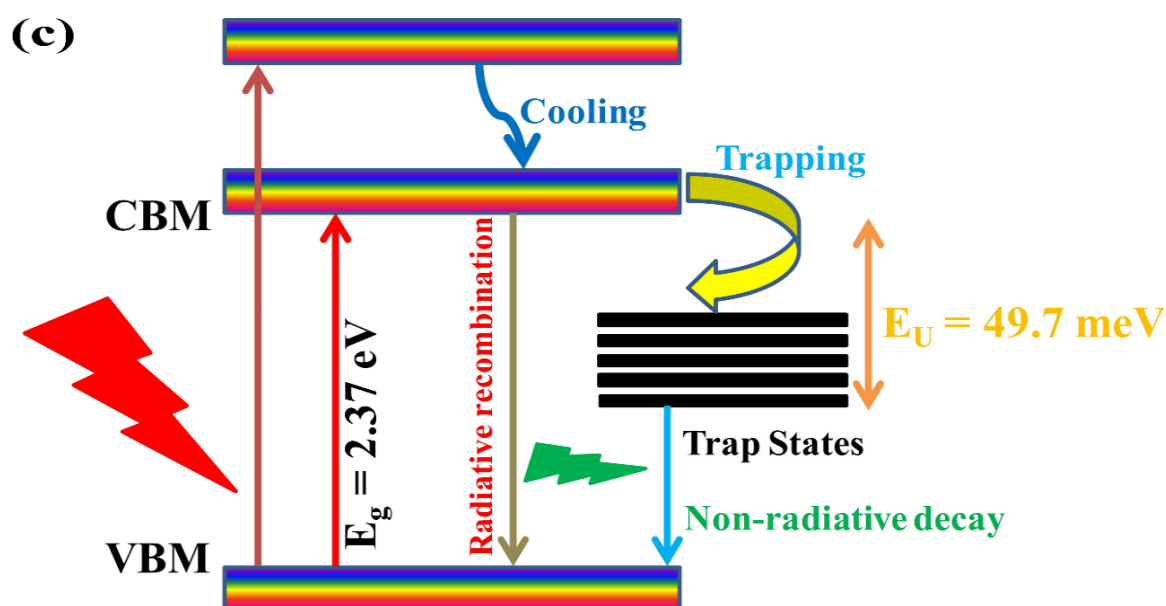
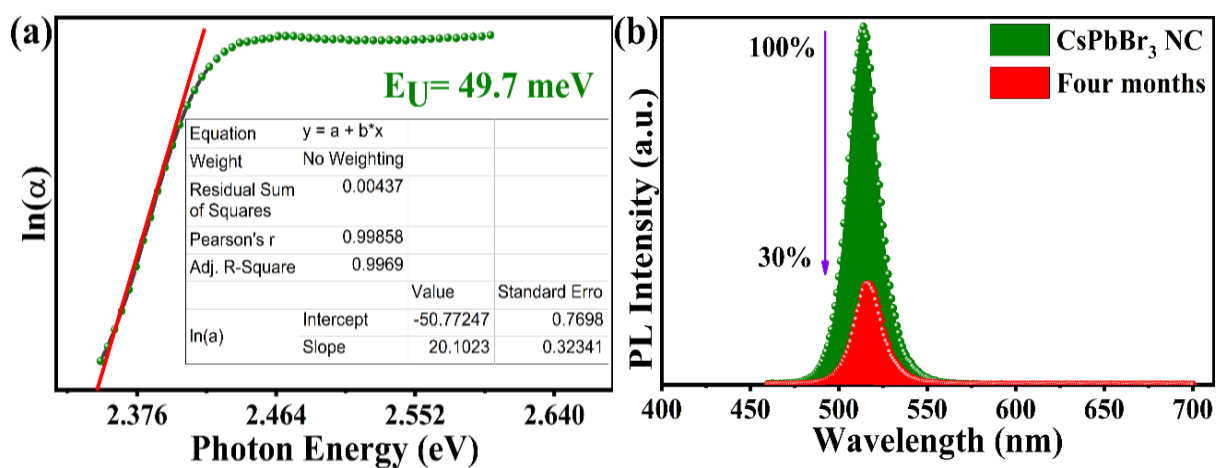


**Figure S8.** (a) Urbach energy fitted diagram; (b) PL degradation spectra; (c) Schematic illustration of Urbach energy through the energy diagram of emissive CsPbBr<sub>3</sub> PNC, respectively.

A large value of the  $E_U$  indicates that the prepared samples contain impurities of cumulative effect, disorders in the inherent structure, and interaction between electron-phonon in the absorption process. For an active light-absorbing material, it has been commonly recognized that the less value of Urbach energy qualifies the material to be used in the photovoltaic devices for attaining high open-circuit voltage. Now, taking the natural logarithm of Eq. (2) we get,

$$\log_e \alpha(E) = \log_e \alpha_0 + \sigma(T) \frac{E-E_0}{k_B T}. \quad (4)$$

The above equation can be re-written as

$$\log_e \alpha(E) = \log_e \alpha_0 - \frac{E_0}{\frac{k_B T}{\sigma(T)}} + \frac{E}{\frac{k_B T}{\sigma(T)}}, \quad (5)$$

Or,

$$\log_e \alpha(E) = \log_e \alpha_0 - \frac{E_0}{E_U} + \frac{E}{E_U}. \quad (6)$$

We can compare Eq. (6) with the straight-line equation such as  $Y = mX + C$ , from where we obtain important parameters like

$$\text{Slope}(m) = \frac{1}{E_U} = \frac{\sigma(T)}{k_B T}; \text{ Intercept } (C) = \log_e \alpha_0 - \frac{E_0}{E_U}, \text{ and } Y(x) = \log_e \alpha(E)$$

The exponential tail using Eq. (2) was fitted to deduce the Urbach energy for CsPbBr<sub>3</sub> PNC and the value comes out to be 47.9 meV. As presented in **Figure S8b**, with the time i.e. four months (as recorded by us), We have also observed a decrease in PL Intensity of CsPbBr<sub>3</sub> PNC. This degradation in intensity directly indicates that material has undergone boundary defects and electronic density disorders [18]. There is a further need to explore the fundamental causes behind the degradation of PL intensity, and a schematic diagram as shown in **Figure S8c**.

## The manual calculation for Urbach Energy

Now, the calculation for Urbach Energy is given below

$$m = \frac{Y_2 - Y_1}{X_2 - X_1} = \frac{-1.515908 - (-2.32)}{2.40 - 2.36} = \frac{0.804092}{0.04}$$

So, we have the value of  $Slope(m)$

$$m = 20.1023 \left(\frac{1}{eV}\right)$$

$$\begin{aligned} E_U &= \frac{1}{m} (eV) = \frac{1}{20.1023} eV \\ &= 0.0497 eV, E_U = 49.7 meV \end{aligned}$$

## **Time-resolved photoluminescence (TRPL)**

We have studied the excited-state kinetics (*i.e.* the spectra of TRPL) of inorganic CsPbBr<sub>3</sub> PNC by time-correlated single-photon counting. From the PL decay curve, as presented in **Figure 2d** (details in the manuscript), PL decay lifetime was calculated.

The values obtained in **Table S2** were recorded by TRPL spectroscopy and can be nicely-fitted and depicted by tri-exponential function

$$I(t) = \alpha + \gamma_1 \exp\left(-\frac{t}{\tau_1}\right) + \gamma_2 \exp\left(-\frac{t}{\tau_2}\right) + \gamma_3 \exp\left(-\frac{t}{\tau_3}\right). \quad (7)$$

Where,  $I(t)$  is the relative intensity at time  $t$  of multi-exponential (tri-exponential) fluorescence decay,  $\tau_i$  is the fluorescence decay lifetimes,  $t$  represents the decay time,  $\gamma_i$  are the amplitude fractions and  $\alpha$  is a specific constant [19,20-25].

The relative factor 'β' can be evaluated with the help of the following relation

$$\beta_i = \frac{\gamma_i}{\sum_{i=1}^3 \gamma_i}. \quad (8)$$

Also, the lifetime (average life-time)  $\tau_{avg}$  can be computed with the help of the following relation [19,20]

$$\tau_{avg} = \sum_{i=1}^3 \beta_i \tau_i. \quad (9)$$

The decay lifetime ( $\tau_1$ ) and its value is shown in **Table S2** [21]. The long-lived lifetime  $\tau_3$  maybe a result of less non-radiative energy transfer to the trap states of inorganic CsPbBr<sub>3</sub>PNC which were synthesized at a high temperature of 180 °C [6,19-25]. The short-lived lifetime of the radiative recombination is the result of superior photoluminescence quantum yields (PLQYs) [6]. We have discussed as well about PLQY in detail (i.e. calculations) as details given in **Figure S6-7**, **Table S1**. In our case ( $\tau_1$ ) is more than five times lower than ( $\tau_2$ ) for the greenish inorganic CsPbBr<sub>3</sub>PNC which is part of the reason for its superior PLQYs i.e. (38.6%) as exhibited in **Table S1** [6]. Now, by using PLQYs and  $\tau_{avg}$  as shown in **Table S2** using the following Eqs. (10) and (11), respectively [22,26].

$$PLQY = \kappa_r / (\kappa_r + \kappa_{nr}) \quad (10)$$

$$\tau_{avg} = 1 / (\kappa_r + \kappa_{nr}) \quad (11)$$

We can calculate the radiative and non-radiative recombination rates as listed values in **Table S3** [22,26].

### Ultrafast transient absorption spectroscopy

With the onset of ultrafast lasers with pulse-width in the femtosecond regime, investigation of photo-physical reactions in real-time added new dimensions to the cutting-edge research areas. In this work, we have also done a comprehensive study on the fundamentals of the transient absorption (TA) technique. The principle of ultrafast TA spectroscopy states that as a result of

an incident pump pulse, a small number of molecules/particles (0.1% to 10%) from the sample get to the excited state. With a delay time  $\tau$  in respect of the pump pulse, a probe pulse is then incident on the specimen. As depicted in **Figure S9**, we can look into the fundamental mechanism of the TA spectroscopy [27]. The advantage of TA spectroscopy over time-resolved fluorescence spectroscopy is that it helps to understand the underlying mechanism of the unfolding of dark states and the non-emissive states. Typically, in an  $\Delta A(\lambda, \tau)$  spectrum following kind of physical processes occur.

- a) The first step is done by ground-state bleaching (GSB) in which a small quantity of particles has been moved to the high energy state because of the high-intensity pump pulse, correspondingly the number of particles in the low energy state i.e. ground state gets reduced. Thence, absorption by the ground state in the exciting part of the sample is much less than in the non – excited sample. Accordingly, an insight picture of the mechanism i.e. a negative signature in the  $\Delta A(\lambda, \tau)$  spectrum is observed in the domain of the ground state absorption displayed in **Figure S9a** [27] as per the principle of the TA spectroscopy. From **Figure S9a**, the difference in absorption spectrum ( $\Delta A$ ) i.e.  $\Delta A = A^* - A$  can be computed, where,  $A^*$  is the absorption of the specimen into the excited state (green) and  $A$  is the ground state (red) absorption.
- b) Due to interaction with the probe pulse, stimulated emission is another step after GSB in TA spectroscopy. Einstein coefficients,  $B_{12}$  and  $B_{21}$ , represent the stimulated absorption coefficient from ground state  $S_0$  (corresponding energy  $E_0$ ) to excited state  $S_1$  (corresponding energy  $E_1$ ) and stimulated emission coefficient from excited state  $S_1$  to ground state  $S_0$ , respectively, which are constant characteristics of the atom. Except for certain non-degeneracy of the quantum energy states that refers to the discrete energy levels like  $S_0$  and  $S_1$  as exhibited in **Figure S9b** [27], these two coefficients are equal i.e.  $B_{12} = B_{21}$ . Optically allowed transitions appear due to stimulated emission only and corresponding fluorescence spectra of the excited fluorescent

specimen will be Stokes shifted with respect to the ground state bleach. In the process of stimulated emission, a quantum of energy from the probe pulse interacting with the excited atomic states gives rise to another quantum of energy while the atom relaxes to the lower state.

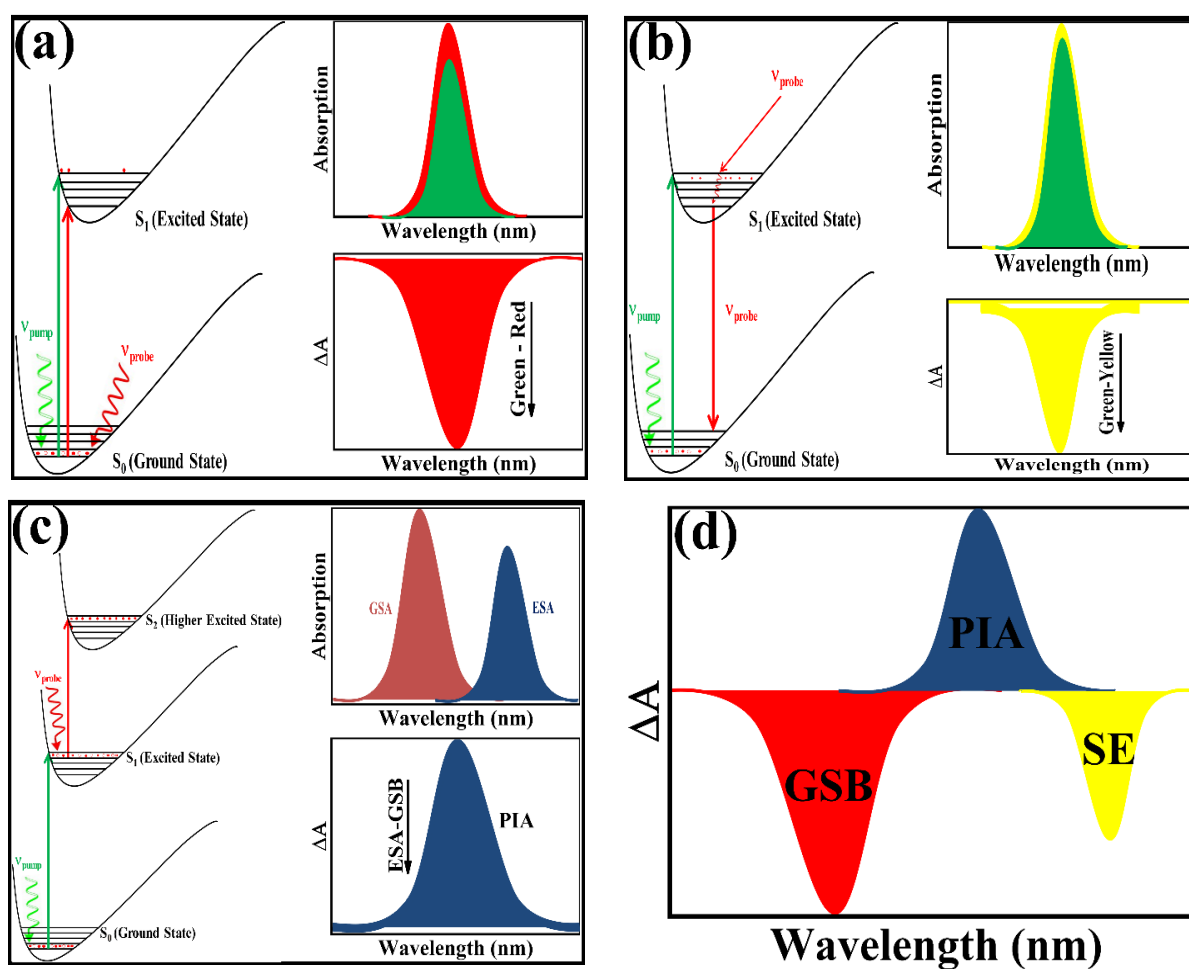


**Figure S9.** Schematic depiction of the fundamental mechanisms of the transient absorption (TA) spectroscopy: (a) GSB, (b) SE, (c) PIA, (d) Schematic depiction of the profile of (fs-TA) spectroscopy, respectively.

Thus, an increase in the intensity of the light detected on the detector corresponds to a kind of negative signature in the difference of absorption spectrum of excited molecules *i.e.*  $\Delta A(\lambda, \tau)$  as exhibited in **Figure S9b**.  $\Delta A = a^* - a$ , where  $a^*$  and  $a$  denote stimulated absorption rates of the excited states and non-excited states, respectively. From these two physical processes, one can conclude that the fluorescent spectra result from the stimulated emission with reduced magnitude and stoke shifted with respect to GSB and sometimes degenerates into the same band [27].

- c) The excited-state absorption (ESA) or photo-induced absorption (PIA) is another important step to make feasible the mechanism of TA in a more comprehensible manner. With the effect of the Pump beam as an excitation source, optically allowed transitions from the higher energy states (high populated state) to higher excited states (less populated) of fluorescence material may occur in the regions of certain distinct wavelengths and at these wavelengths, absorptions of probe pulse will occur. Therefore, positive signaling will occur in the difference of absorption ( $\Delta A(\lambda, \tau)$ ) at these specified wavelengths of the excited-state absorption (or photo-induced absorption) as demonstrated in **Figure S9c** [27]. This can be seen in the schematic diagram (**Figure S9d**) that by varying the delay time  $\tau$  between the pump and probe pulses, the difference in absorption ( $\Delta A$ ) as a function of delay time  $\tau$  and wavelength ( $\lambda$ ) *i.e.*  $\Delta A(\lambda, \tau)$  can be constructed [27].

## Structural stability test

All-inorganic CsPbBr<sub>3</sub> PNC are attractive candidates for practical device applications by virtue of their high degree of stability in comparison with other similar structured compounds as well as organic-inorganic hybrid PNCs e.g. MAPbX<sub>3</sub> (MA = CH<sub>3</sub>NH<sub>3</sub>, X = Cl, Br, and I) when exposed to heat or moisture at room temperature [2]. Herein, we have studied the structural stability of all-inorganic CsPbBr<sub>3</sub> PNC over nine months under an inert atmosphere, our analysis shows that there is no loss of morphology of the PNC. Furthermore, the composition of material remains unchanged over the said time duration and does not disintegrate into PbBr<sub>2</sub> and other by-products as depicted in **Figure S10a-b**. Although slightly changed intensity of XRD peaks, but remain unchanged the characteristic peaks, as shown in **Figure S10a** and can be verified with the image in **Figure S1** (Supporting Information) [14]. No change occurs in cubic morphology which is further confirmed by acquiring TEM images after nine months as shown in **Figure S10b** and can be verified with the image in **Figure S2c**. The structural stability and unchanged morphology over nine months make CsPbBr<sub>3</sub> PNC a perfect candidate for novel future device applications such as the fabrication of novel all-optical devices [14]. It has been well established that the continuous exposure to air, moisture, and light can lead to degradation of PNC, so it is imperative to put the films of PNC in an inert atmosphere, such that they can be used for various device applications such as photo-detectors, LEDs, and lasers [28].

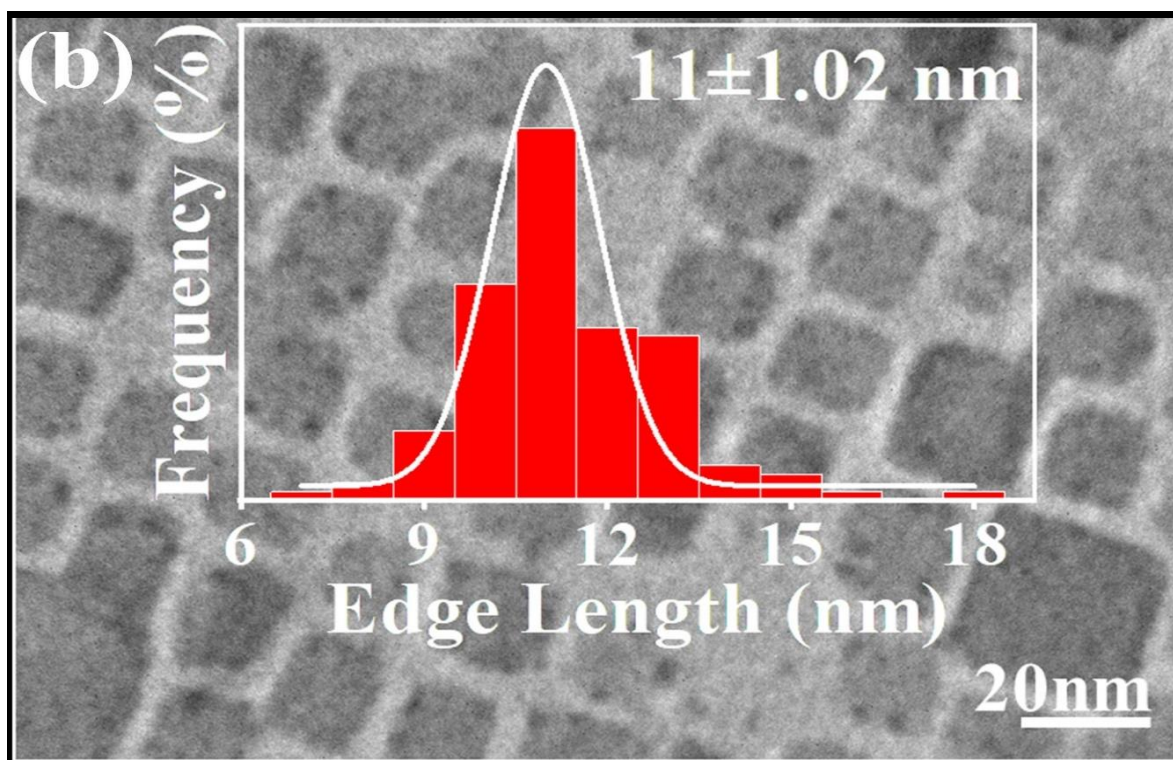
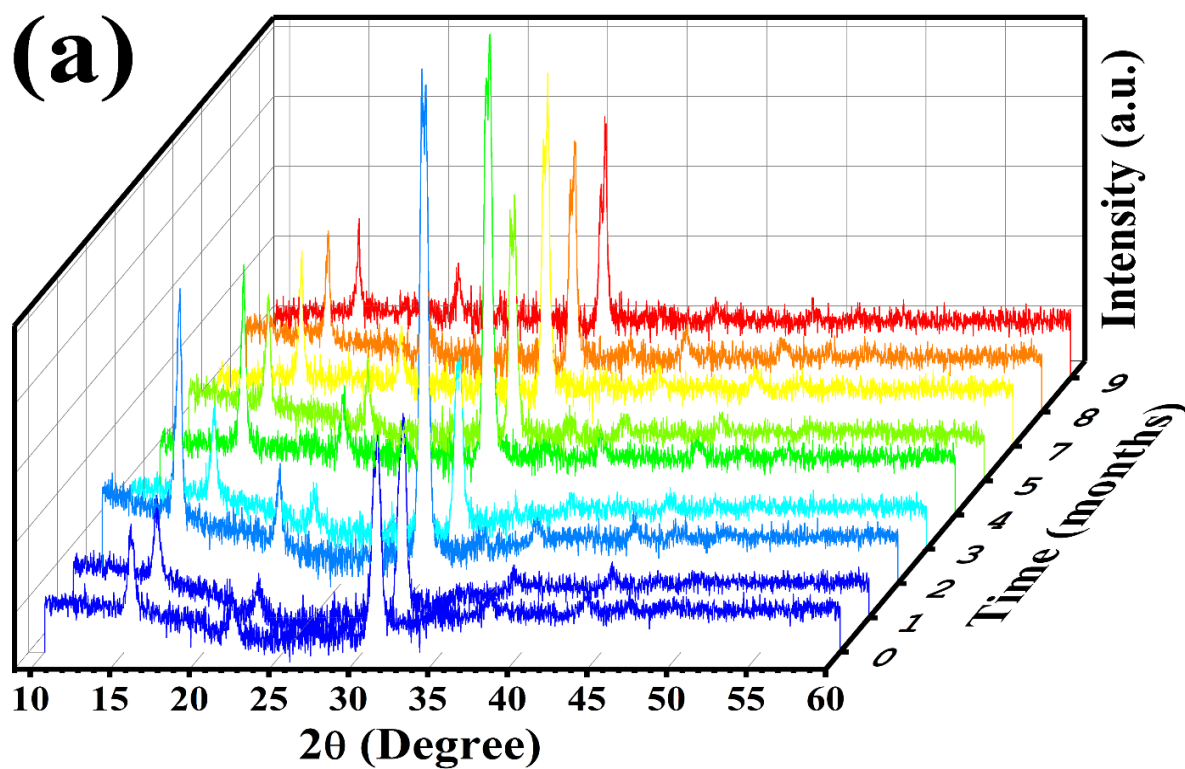


**Figure S10.** Photographs are depicting the stability of CsPbBr<sub>3</sub> PNC when stored into the inert ambience for the nine months; (a) XRD pattern showing the stability of CsPbBr<sub>3</sub> PNC; (b) The TEM image of CsPbBr<sub>3</sub> PNC is putting forward that the no loss of morphology and size of PNC.

**Table S1.** Extracted data from measurements of the absorption and integrated photoluminescence spectra.

| Fluorescein Dye |            | CsPbBr <sub>3</sub> PNC |            | PLQY% of CsPbBr <sub>3</sub> PNC |
|-----------------|------------|-------------------------|------------|----------------------------------|
| 0.020           | 10478.6648 | 0.023                   | 5000.866   | 38.6                             |
| 0.043           | 26751.9467 | 0.040                   | 10335.3273 |                                  |
| 0.061           | 39302.7832 | 0.066                   | 15994.3507 |                                  |
| 0.087           | 49111.4972 | 0.086                   | 20273.7244 |                                  |
| 0.101           | 65030.1489 | 0.104                   | 25508.6797 |                                  |

**Table S2.** The decay constants for time-resolved photoluminescence and the rates for radiative and non-radiative recombination of the CsPbBr<sub>3</sub> PNC.

| Sample                     | $\tau_1/$<br>(10 <sup>-9</sup> s) | $\beta_1\%$ | $\tau_2/$<br>(10 <sup>-9</sup> s) | $\beta_2\%$ | $\tau_3/$<br>(10 <sup>-9</sup> s) | $\beta_3\%$ | $\tau_{\text{average}}$<br>(10 <sup>-9</sup> s) | $\chi^2$ |
|----------------------------|-----------------------------------|-------------|-----------------------------------|-------------|-----------------------------------|-------------|-------------------------------------------------|----------|
| CsPbBr <sub>3</sub><br>PNC | 4.72                              | 42.9        | 25.95                             | 43.5        | 80.52                             | 13.6        | 24.20                                           | 1.107    |

**Table S3.** Radiative transition rate ( $\kappa_r$ ), non-radiative transition rate ( $\kappa_{nr}$ ) and ratio  $\kappa_r/\kappa_{nr}$  of the CsPbBr<sub>3</sub> PNC.

| Sample                  | $\kappa_r$<br>(10 <sup>6</sup> s <sup>-1</sup> ) | $\kappa_{nr}$<br>(10 <sup>6</sup> s <sup>-1</sup> ) | $\kappa_r/\kappa_{nr}$ | Ref.      |
|-------------------------|--------------------------------------------------|-----------------------------------------------------|------------------------|-----------|
| CsPbBr <sub>3</sub> PNC | 6.98                                             | 11.8                                                | 0.59                   | 30        |
| CsPbBr <sub>3</sub> PNC | 15.95                                            | 25.37                                               | 0.63                   | This work |

**Table S4.** TA decay parameters at different powers of the femtosecond laser system of the CsPbBr<sub>3</sub> NC.

| Sample                     | P/mW | $\lambda/\text{nm}$ | $\tau_1/10^{-12}\text{s}$ | $A^*_1\%$ | $\tau_2/10^{-12}\text{s}$ | $A^*_2\%$ | $\tau_3/10^{-12}\text{s}$ | $A^*_3\%$ | $\tau_{\text{average}}/10^{-12}\text{s}$ |
|----------------------------|------|---------------------|---------------------------|-----------|---------------------------|-----------|---------------------------|-----------|------------------------------------------|
| CsPbBr <sub>3</sub><br>PNC | 0.10 | 511                 | 0.760                     | 30.4      | 85.6                      | 48.8      | 1987.32                   | 20.8      | 455.37                                   |
| CsPbBr <sub>3</sub><br>PNC | 0.30 | 511                 | 0.61                      | 34.6      | 175.56                    | 45.6      | 4059.50                   | 19.8      | 884.05                                   |

**Table S5.** Radiative transition rate ( $\kappa_r$ ), non- radiative transition rate ( $\kappa_{nr}$ ) and ratio  $\kappa_r/\kappa_{nr}$  of the CsPbBr<sub>3</sub> PNC using the Transient Absorption spectroscopy.

| Sample                     | P/mW | $\lambda/\text{nm}$ | $\kappa_r (10^9\text{s}^{-1})$ | $\kappa_{nr} (10^9\text{s}^{-1})$ | $\kappa_r/\kappa_{nr}$ |
|----------------------------|------|---------------------|--------------------------------|-----------------------------------|------------------------|
| CsPbBr <sub>3</sub><br>PNC | 0.10 | 511                 | 0.84                           | 1.35                              | 0.62                   |
| CsPbBr <sub>3</sub><br>PNC | 0.30 | 511                 | 0.44                           | 0.69                              | 0.64                   |

**Table S6.** Binding energies and computed various parameters for different core levels as administered in Figure S1.

| Element | Core level | Binding Energy (eV) | FWHM  | Area         | At%   | Spin Orbit Splitting Energy (eV) | Area Ratio | Br:Pb / Br:Cs | Cs:Pb:Br  |
|---------|------------|---------------------|-------|--------------|-------|----------------------------------|------------|---------------|-----------|
| Cs 3d   | $3d_{3/2}$ | 738.065             | 1.004 | 272.708      | 17.97 | 13.974                           | 3:5        | 2.54/<br>3.3  | 1:1.3:3.3 |
|         | $3d_{5/2}$ | 724.091             | 1.306 | 499.640      |       |                                  |            |               |           |
|         | $4d_{3/2}$ | 77.203              | 0.963 | 209.382      |       | 2.336                            | 2:3        |               |           |
|         | $4d_{5/2}$ | 74.867              | 0.915 | 271.717      |       |                                  |            |               |           |
| Pb 4f   | $4f_{5/2}$ | 142.746             | 0.986 | 851.656      | 23.51 | 4.854                            | 2:3        | 3.3           |           |
|         | $4f_{7/2}$ | 137.892             | 0.918 | 1154.54<br>1 |       |                                  |            |               |           |
| Br 3d   | $3d_{3/2}$ | 68.784              | 0.985 | 282.762      | 59.53 | 1.031                            | 3:4        |               |           |
|         | $3d_{5/2}$ | 67.753              | 0.963 | 369.510      |       |                                  |            |               |           |

## Supporting References

1. F. Liu, Y. Zhang, C. Ding, S. Kobayashi, T. Izuishi, N. Nakazawa, T. Toyoda, T. Ohta, S. Hayase, T. Minemoto, *ACS nano*, 2017, 11, 10373-10383.
2. L. Protesescu, S. Yakunin, M.I. Bodnarchuk, F. Krieg, R. Caputo, C.H. Hendon, R.X. Yang, A. Walsh, M.V. Kovalenko, *Nano Lett.*, 2015, 15, 3692-3696.
3. J. Moulder, W. Stickle, P. Sobol, K. Bomben, G. Muilenberg, Eden Prairie, 1992.
4. H. Liu, Z. Liu, W. Xu, L. Yang, Y. Liu, D. Yao, D. Zhang, H. Zhang, B. Yang, *ACS Appl. Mater. Interfaces*, 2019, 11, 14256-14265.
5. V.K. Ravi, P.K. Santra, N. Joshi, J. Chugh, S.K. Singh, H. Rensmo, P. Ghosh, A. Nag, J. *Phys. Chem. Lett.*, 2017, 8, 4988-4994
6. X. Li, Y. Wu, S. Zhang, B. Cai, Y. Gu, J. Song, H. Zeng, *Adv. Funct. Mater.*, 2016, 26, 2435-2445.
7. C. Ilie, F. Guzman, B. Swanson, I. Evans, P. Costa, J. Teeter, M. Shekhirev, N. Benker, S. Sikich, A. Enders, *J. Phys.: Condens. Matter*, 2018, 30, 18LT02.
8. J. Endres, M. Kulbak, L. Zhao, B.P. Rand, D. Cahen, G. Hodes, A. Kahn, *J. Appl. Phys.*, 2017, 121, 035304.
9. J.F. Moulder, *Phys. Electron.*, 1995, 230-232.
10. P. Chen, Y. Bai, S. Wang, M. Lyu, J.H. Yun, L. Wang, *Adv. Funct. Mater.*, 2018, 28, 1706923.
11. E.M. Sanehira, A.R. Marshall, J.A. Christians, S.P. Harvey, P.N. Ciesielski, L.M. Wheeler, P. Schulz, L.Y. Lin, M.C. Beard, J.M. Luther, *Sci. Adv.*, 2017, 3, eaao4204.
12. Y. Kim, E. Yassitepe, O. Voznyy, R. Comin, G. Walters, X. Gong, P. Kanjanaboos, A.F. Nogueira, E.H., *ACS Appl. Mater. Interfaces*, 2015, 7, 25007-25013.
13. J. Pan, L.N. Quan, Y. Zhao, W. Peng, B. Murali, S.P. Sarmah, M. Yuan, L. Sinatra, N.M. Alyami, J. Liu, *Adv. Mater.*, 2016, 28, 8718-8725.

14. Q. Zhong, M. Cao, H. Hu, D. Yang, M. Chen, P. Li, L. Wu, Q. Zhang, *ACS nano*, 2018, 12, 8579-8587.
15. L. Wu, Q. Zhong, D. Yang, M. Chen, H. Hu, Q. Pan, H. Liu, M. Cao, Y. Xu, B. Sun, *Langmuir*, 2017, 33, 12689-12696.
16. L. Wu, J. Yu, L. Chen, D. Yang, S. Zhang, L. Han, M. Ban, L. He, Y. Xu, Q. Zhang, J. *Mater. Chem. C*, 2017, 5, 3065-3071.
17. H. Shurvell, John Wiley & Sons, Ltd., 2006.
18. J. Zeng, X. Li, Y. Wu, D. Yang, Z. Sun, Z. Song, H. Wang, H. Zeng, *Adv. Funct. Mater.*, 2018, 28, 1804394.
19. D. T. Moore, A.R. Marshall, E.M. Sanehira, J.A. Christian, A. SWARNKAR, B.D. Chernomordik, *Am. Assoc. Adv. Sci.*, 2016, 354, 92-95.
20. L. Tang, R. Ji, X. Li, K.S. Teng, S.P. Lau, *J. Mater. Chem. C*, 2013, 1, 4908-4915.
21. Liang, Zhiqin, Suling Zhao, Zheng Xu, Bo Qiao, Pengjie Song, Di Gao, and Xurong Xu, *ACS Appl. Mater. Interfaces*, 2016, 8, 28824-28830.
22. Tong, Jianyu, Jiajing Wu, Wei Shen, Yukang Zhang, Yao Liu, Tao Zhang, Shuming Nie, and Zhengtao Deng, *ACS Appl. Mater. Interfaces*, 2019, 11, 9317-9325.
23. Sun, Shibin, Dan Yuan, Yuan Xu, Aifei Wang, and Zhengtao Deng, *ACS Nano*, 2016, 10, 3648-3657.
24. Bi, Chenghao, Shixun Wang, Wen Wen, Jifeng Yuan, Guozhong Cao, and Jianjun Tian, *J. Phys. Chem. C*, 2018, 122, 5151-5160.
25. Shi, Huafeng, Xiaoli Zhang, Xiaowei Sun, Rui Chen, and Xinhai Zhang, *J. Phys. Chem. C*, 2019, 123, 19844-19850.
26. J.-F. Liao, Y.-F. Xu, X.-D. Wang, H.-Y. Chen, D.-B. Kuang, *ACS Appl. Mater. Interfaces*, 2018, 10, 42301-42309.
27. R. Berera, R. van Grondelle, J.T. Kennis, *Photosynth. Res.*, 2009, 101, 105-118.

28. K. Pradeep, S. Chakraborty, R. Viswanatha, Mater. Res. Express, 2019, 6, 114004.